

1           The Community Code Verification Exercise for  
2           Simulating Sequences of Earthquakes and Aseismic Slip  
3           (SEAS)

4           Brittany A. Erickson<sup>1\*</sup>, Junle Jiang<sup>2\*</sup>, Michael Barall<sup>3</sup>, Nadia Lapusta<sup>4</sup>,  
Eric M. Dunham<sup>5</sup>, Ruth Harris<sup>6</sup>, Lauren S. Abrahams<sup>5</sup>, Kali L. Allison<sup>7</sup>,  
Jean-Paul Ampuero<sup>8</sup>, Sylvain Barbot<sup>9</sup>, Camilla Cattania<sup>5</sup>, Ahmed Elbanna<sup>10</sup>,  
Yuri Fialko<sup>11</sup>, Benjamin Idini<sup>4</sup>, Jeremy E. Kozdon<sup>12</sup>, Valère Lambert<sup>4</sup>,  
Yajing Liu<sup>13</sup>, Yingdi Luo<sup>4</sup>, Xiao Ma<sup>10</sup>, Maricela Best McKay<sup>14</sup>,  
Paul Segall<sup>5</sup>, Pengcheng Shi<sup>15</sup>, Martijn van den Ende<sup>8</sup>, Meng Wei<sup>15</sup>

<sup>1</sup>University of Oregon, 1477 E. 13th Ave., Eugene , OR 97403-1202

<sup>2</sup>Cornell University

<sup>3</sup>Invisible Software

<sup>4</sup>California Institute of Technology

<sup>5</sup>Stanford University

<sup>6</sup>United States Geological Survey

<sup>7</sup>University of Maryland

<sup>8</sup>Université Côte d’Azur, IRD, CNRS,  
Observatoire de la Côte d’Azur, Géoazur, France

<sup>9</sup>University of Southern California

<sup>10</sup>University of Illinois Urbana-Champaign

<sup>11</sup>University of California San Diego

<sup>12</sup>Naval Postgraduate School

<sup>13</sup>McGill University

<sup>14</sup>Portland State University

<sup>15</sup>University of Rhode Island

5           September 4, 2019

---

\*Correspondence to B.A.E (bae@uoregon.edu) and J.J. (jjiang@cornell.edu)

- 6 Any use of trade, firm, or product names is for descriptive purposes only and does not
- 7 imply endorsement by the U.S. Government.

## Abstract

Numerical simulations of Sequences of Earthquakes and Aseismic Slip (SEAS) have made great progress over the past decades to address important questions in earthquake physics and fault mechanics. However, significant challenges in SEAS modeling remain in resolving multiscale interactions between aseismic fault slip, earthquake nucleation, and dynamic rupture; and understanding physical factors controlling observables such as seismicity and ground deformation. The increasing capability and complexity of SEAS modeling calls for extensive efforts to verify codes and advance these simulations with rigor, reproducibility, and broadened impact. In 2018, we initiated a community code-verification exercise for SEAS simulations, supported by the Southern California Earthquake Center (SCEC). Here we report the findings from our first two benchmark problems (BP1 and BP2), designed to test the capabilities of different computational methods in correctly solving a mathematically well-defined, basic problem in crustal faulting. These benchmarks are for a 2D antiplane problem, with a 1D planar vertical strike-slip fault obeying rate-and-state friction, embedded in a 2D homogeneous, linear elastic half-space. Sequences of quasi-dynamic earthquakes with periodic occurrences (BP1) or bimodal sizes (BP2) and their interactions with aseismic slip are simulated. The comparison of  $>70$  simulation results from 11 groups using different numerical methods, uploaded to our online platform, show excellent agreements in long-term and coseismic evolution of fault properties. In BP1, we found that the truncated domain boundaries influence interseismic fault stressing, earthquake recurrence, and coseismic rupture process, and that agreement between models is only achieved with sufficiently large domain sizes. In BP2, we found that complexity of long-term fault behavior depends on how well important physical length scales related to spontaneous nucleation and rupture propagation are resolved. Poor numerical resolution can result in the generation of artificial complexity, impacting simulation results that are of potential interest for characterizing seismic hazard, such as earthquake size distributions, moment release, and earthquake recurrence times. These results inform the development of more advanced SEAS models, contributing to our further understanding of earthquake system



## Introduction and Motivation

When we develop models of physical systems, credible and reproducible results are essential to scientific progress. Robust predictive models of earthquake source processes have become important means for studying fundamental questions in earthquake science. Models of single earthquakes (known as *dynamic rupture simulations*) have emerged as powerful tools for understanding the influence of fault geometry, friction and prestress on rupture propagation, and for explaining observations of high-frequency ground motions and damage zones (Day, 1982; Olsen et al., 1997; Nielsen et al., 2000; Duan and Oglesby, 2006; Ripperger et al., 2007; Bhat et al., 2007; Dunham et al., 2011a,b; Lozos et al., 2011; Gabriel et al., 2012; Shi and Day, 2013; Kozdon and Dunham, 2013; Xu et al., 2015; Wollherr et al., 2018; Ma and Elbanna, 2019). Many of the codes used for these studies incorporate advanced features such as 3D domains and complex fault geometries, leading to very large problems for which rigorous convergence tests can be too computationally expensive. An alternative means for verifying model results are code comparisons made across the different modeling groups, using cell sizes at the limit of computational feasibility. Over the past decade, the SCEC/USGS Spontaneous Rupture Code Verification Project has made significant progress in using code comparison studies to provide confidence in model outcomes (Harris et al., 2009; Barall and Harris, 2015; Harris et al., 2018).

Although these dynamic rupture simulations have contributed greatly to our understanding of the physical factors that govern ground motion, they are limited to single-event scenarios with imposed artificial prestress conditions and *ad hoc* nucleation procedures. In order to understand earthquake source processes and how fault slip history influences subsequent events, it has been widely recognized that we need models that simulate behavior over multiple seismic events and the intervening periods of aseismic deformation. To address this need, models of Sequences of Earthquakes and Aseismic Slip (SEAS) have emerged that consider all phases of earthquake faulting, from slow tectonic loading to earthquake nucleation (under self-consistent prestress

66 conditions), propagation and termination. However, so far codes for SEAS simulations  
67 remain untested. Inspired by the success of the SCEC/USGS Spontaneous Rupture  
68 Code Verification Project, this paper describes the efforts of the SEAS initiative – a  
69 SCEC (Southern California Earthquake Center) funded working group who has initi-  
70 ated the first code-verification study for earthquake sequence simulations. In this pa-  
71 per, we present the initial benchmark problems and results from the code comparisons  
72 submitted to our online platform (<http://sceccdata.usc.edu/cvws/seas/>). Through  
73 these exercises, we aim to provide confidence in SEAS model outcomes, determine best  
74 practices for improvement of accuracy and efficiency of SEAS simulations, and provide  
75 other scientists strategies for verification during code development.

76 In SEAS models the goal is to capture the interplay of interseismic periods and  
77 the associated aseismic fault slip that ultimately lead to earthquake nucleation and  
78 earthquakes (dynamic rupture events) themselves, in an effort to understand which  
79 physical factors control the full range of observables such as aseismic deformation,  
80 nucleation locations of earthquakes, ground shaking during dynamic rupture, recurrence  
81 times and magnitudes of major earthquakes, see Figure 1. These features distinguish  
82 SEAS models from both dynamic rupture models which only consider single events,  
83 and the so-called earthquake simulators (*Tullis et al.*, 2012). Earthquake simulators are  
84 capable of simulating seismicity patterns over millennium time scales in complex fault  
85 network systems (*Richards-Dinger and Dieterich*, 2012) but are missing key physical  
86 features that could potentially dominate earthquake and fault interaction, such as stress  
87 transfer generated by dynamic waves, aseismic slip within fault segments, and inelastic  
88 responses.

89 SEAS modeling is not without significant challenges, due to the varying tempo-  
90 ral and spatial scales that characterize earthquake source behavior. For computational  
91 efficiency the vast majority of SEAS models do not consider full dynamics during earth-  
92 quake rupture, but rather take a "quasi-dynamic" approach, where inertia is only ap-  
93 proximated (see section for further details). Computations are further complicated  
94 when material heterogeneities, bulk inelastic responses and fault nonplanarity are in-

95 cluded. However, accounting for such complexity is widely recognized as crucial for  
96 understanding the real Earth and predicting seismic hazards. Significant developments  
97 in SEAS models over the past decade have incorporated some of these complexities and  
98 connected model outcomes to geophysical observations. For example, seismological and  
99 geodetic observations have been combined with modeling of coseismic and quasi-static  
100 (aseismic) deformation to infer the spatial distribution of fault frictional properties  
101 (*Johnson et al.*, 2006; *Barbot et al.*, 2009; *Mitsui and Hirahara*, 2011; *Dublanchet et al.*,  
102 2013; *Floyd et al.*, 2016; *Jiang and Fialko*, 2016), the decay rate of aftershocks (*Per-*  
103 *fettini and Avouac*, 2004, 2007), the role of tremor and slow slip (*Mele Veedu and*  
104 *Barbot*, 2016; *Dublanchet*, 2017; *Luo and Ampuero*, 2017), and long-term models have  
105 been used to reproduce characteristics of multiple and/or repeating events (*Chen and*  
106 *Lapusta*, 2009; *Barbot et al.*, 2012). The framework of earthquake cycle modeling is  
107 also adopted to explain geodetic and geologic data (*Meade et al.*, 2013; *Kaneko et al.*,  
108 2011; *Wei et al.*, 2013, 2018), study subduction zones (*Hori et al.*, 2004; *van Dinther*  
109 *et al.*, 2013; *Noda and Lapusta*, 2013; *Liu and Rice*, 2005, 2007; *Li and Liu*, 2016,  
110 2017), collision zones (*Qiu et al.*, 2016; *Michel et al.*, 2017), and explore induced seis-  
111 micity phenomena (*McClure and Horne*, 2011; *Dieterich et al.*, 2015), among many  
112 applications.

113 While SEAS models are being used to explain, reproduce, and predict earthquake  
114 behavior and other geophysical phenomena, a critical step must be to ensure that these  
115 methodologies are accurate. The SEAS initiative is also taking the step to improve  
116 and promote a new generation of verified numerical SEAS models that can simulate  
117 much longer periods of earthquake activity than single-event dynamic rupture simula-  
118 tions but with the same level of computational rigor, while incorporating qualitatively  
119 different features such as (a) pre-, inter-, and post-seismic slip and the resulting stress  
120 redistribution, (b) spontaneous earthquake nucleation, and (c) physical processes rele-  
121 vant to long-term slip such as interseismic healing of the fault zone, viscoelasticity, and  
122 fluid flow. Such SEAS models can provide physics-based approximations for larger-scale  
123 and longer-term earthquake simulators. In addition they can inform the initial condi-

124 tions and nucleation procedures for dynamic rupture simulations, however our vision  
125 for SEAS models is to develop them all to include full dynamic ruptures, capturing the  
126 range of processes and heterogeneities known to be essential for realistic ground motion  
127 modeling.

## 128 SEAS Modeling Challenges and Initial Benchmark 129 Problems

130 Although the ultimate SEAS modeling framework would naturally include dynamic rup-  
131 ture modeling, current methods for simulating SEAS problems require computational  
132 codes that are fundamentally different from those used in single-event dynamic rupture  
133 simulations. The use of variable time stepping and possible switching between different  
134 computational schemes is required in order to resolve sub-seconds to year-long changes.  
135 The interaction between the highly nonlinear nature of the problems and round-off er-  
136 rors can lead to model divergence. The need to distinguish between legitimate solution  
137 differences due and improper choices of algorithm and modeling procedures necessitates  
138 new and more suitable comparison metrics.

139 SEAS models are unique in that they cover a wide range of numerical methodologies  
140 and applications in earthquake science. Methods based on spectral boundary integral  
141 formulations (BIEM) are efficient in solving for earthquake ruptures with quasi-dynamic  
142 or full inertial effects (*Lapusta and Rice, 2003; Lapusta and Liu, 2009; Jiang and La-*  
143 *pusta, 2016*). Methods based on the finite difference method (FDM) or a hybrid finite  
144 element/spectral BIEM have been used to simulate quasi-dynamic ruptures on faults  
145 with more complex bulk rheologies (*Erickson and Dunham, 2014; Erickson et al., 2017;*  
146 *Allison and Dunham, 2018; Mckay et al., 2019; Abdelmeguid et al., 2019*). Other SEAS  
147 modeling approaches include boundary element methods (BEM) for simulating slow slip  
148 and tremor (e.g., *Tse and Rice, 1986; Rice and Tse, 1986; Ong et al., 2019; Goswami*  
149 *and Barbot, 2018; Luo and Ampuero, 2011; Nakata et al., 2012; Liu, 2013; Wei et al.,*



2013), coupling faulting with fluid/heat transport and inelastic dilatancy (*Segall and Bradley, 2012a*), effects of surface topography (*Ohtani and Hirahara, 2015*), frictional heterogeneities (*Kato, 2016*) and viscoelastic response (*Kato, 2002; Lambert and Barbot, 2016; Barbot, 2018*). A spectral element method (SEM) has also been developed for simulating fully dynamic earthquakes in a heterogeneous bulk (*Kaneko et al., 2010*).

To verify the accuracy of SEAS models based on these different computational methods, the SEAS group developed our first benchmark problem, BP1, to test the capabilities of different computational methods in correctly solving a mathematically well-defined problem in crustal faulting. The overall strategy of our benchmark exercises is to produce robust results and maximize participation, with the goal of obtaining agreements in resolving detailed fault slip history over a range of time scales. These efforts required us to better understand the dependence of fault slip history on initial conditions, model spin-up, fault properties, and friction laws. Given the complexity of this task, it was important to start from the most basic problem and gradually add model complexity. BP1 is a 2D antiplane problem, with a 1D planar vertical strike-slip fault embedded in a 2D homogeneous, linear elastic half-space with a free surface, see Figure 2. Full details of this benchmark (and subsequent benchmarks), including governing equations and initial and fault interface conditions, are available online on the SEAS platform (<http://scecddata.usc.edu/cvws/seas/index.html>). We include some of the details on the friction law here, for clarity of important concepts.

The fault is governed by rate- and state-dependent friction (*Dieterich, 1979; Ruina, 1983; Marone, 1998*) where shear stress on the fault  $\tau$  is set equal to fault strength  $F$ , namely

$$\tau = F(V, \theta), \tag{1}$$

where  $\tau = \tau^0 + \tau^{\text{qs}} - \eta V$  is the sum of the prestress  $\tau^0$ , the shear stress due to quasi-static deformation  $\tau^{\text{qs}}$ , and the radiation damping term  $-\eta V$  as approximation to inertia (*Rice, 1993*).  $\eta = \mu/2c_s$  is half the shear-wave impedance for shear wave speed  $c_s = \sqrt{\mu/\rho}$ , where  $\mu$  is the elastic shear modulus and  $\rho$  is the material density. The

178 fault strength  $F = \sigma_n f(V, \theta)$ , where  $V$  is the slip rate and  $\theta$  is a state variable.  $\sigma_n$  is  
 179 the effective normal stress on the fault. For this first benchmark problem we assume  $\theta$   
 180 evolves according to the aging law

$$181 \quad \frac{d\theta}{dt} = 1 - \frac{V\theta}{L}, \quad (2)$$

182 where  $L$  is the critical slip distance. The friction coefficient  $f$  is given by a regularized  
 183 formulation (*Lapusta et al.*, 2000)

$$184 \quad f(V, \theta) = a \sinh^{-1} \left[ \frac{V}{2V_0} \exp \left( \frac{f_0 + b \ln(V_0\theta/L)}{a} \right) \right] \quad (3)$$

185 for reference friction coefficient  $f_0$  and reference slip rate  $V_0$ . Depth-dependent fric-  
 186 tional parameters  $a$  and  $b$  define a shallow seismogenic region with velocity-weakening  
 187 (VW) friction and a deeper velocity-strengthening (VS) region, below which a rela-  
 188 tive plate motion rate is imposed. A periodic sequence of spontaneous, quasi-dynamic  
 189 earthquakes and slow slip are simulated in the model, see Figure 3a, where results from  
 190 the BICyclE code (*Lapusta et al.*, 2000; *Lapusta and Liu*, 2009) show slip contours plot-  
 191 ted against fault depth in blue every 5 yr during interseismic loading and in red every  
 192 1 s during the coseismic phase. Over a 1200 year simulation period, approximately 13  
 193 events take place, nucleating at a depth of  $\sim 12$  km, rupturing to a depth of  $\sim 18$  km,  
 194 and accumulating  $\sim 3$  m of slip at the Earth’s surface. Model parameters used for the  
 195 benchmark are given in Table 1.

196 A critical physical length scale present in this first benchmark problem, often re-  
 197 ferred to as the process zone or cohesive zone  $\Lambda$ , describes the spatial region near the  
 198 rupture front under which breakdown of fault resistance occurs, and shrinks as ruptures  
 199 propagate faster (*Palmer and Rice*, 1973). For fault models governed by rate-and-state  
 200 friction, the quasi-static process zone at a rupture speed of  $0^+$ ,  $\Lambda_0$ , can be estimated  
 201 (*Day et al.*, 2005; *Ampuero and Rubin*, 2008; *Perfettini and Ampuero*, 2008) as

$$202 \quad \Lambda_0 = C \frac{\mu L}{b\sigma_n}, \quad (4)$$

203 where  $C$  is a constant of order 1. Another characteristic length scale which has been  
 204 shown to control model behavior is the critical nucleation size  $h^*$ , which governs the  
 205 minimum extent of the rate-weakening region under which spontaneous nucleation may  
 206 occur, (see *Andrews, 1976a,b; Rubin and Ampuero, 2005; Ampuero and Rubin, 2008*).  
 207 For 2D problems, the critical nucleation size can be estimated for the aging law (with  
 208  $0.5 < a/b < 1$ ) as

$$209 \quad h^* = \frac{2}{\pi} \frac{\mu b L}{(b-a)^2 \sigma_n}. \quad (5)$$

210 A cell size of 50 m was used for BP1, resolving  $\Lambda_0$  with approximately 6 grid points and  
 211  $h^*$  with approximately 40 grid points.

212 We developed the second benchmark BP2 that is similar to BP1 to explore the  
 213 model resolution issues, which will be important in future benchmarks in 3D when  
 214 computational efficiency demands a larger cell size. Complexity of event sizes and  
 215 recurrence times is known to emerge through a reduction in the characteristic slip  
 216 distance  $L$  (*Lapusta and Rice, 2003; Mitsui and Hirahara, 2011; Wu and Chen, 2014;*  
 217 *Kato, 2014; Barbot, 2019; Viesca, 2016a,b; Cattania, 2019*). Thus BP2 is exactly the  
 218 same as BP1 except that  $L$  is halved, resulting in bimodal sequences of full and partial  
 219 ruptures of the velocity-weakening region (every large event is accompanied by a smaller  
 220 event and the sequence repeats periodically). Besides aiming for agreements between  
 221 different models, one main objective is to understand complexity in simulated events  
 222 and how to deal with numerical resolution issues. A reduction in  $L$  corresponds to a  
 223 reduction in the quasi-static process zone size  $\Lambda_0$ . BP2 requests model outputs using  
 224 a cell size of 25 m, 50 m, 100 m, 200 m, 300 m, 400 m and 800 m. The first three cases  
 225 resolve  $\Lambda_0$  with approximately 6, 3, and 1.7 grid points, and the other four cases do  
 226 not resolve  $\Lambda_0$ . Figures 3b-d show results from the BICycle code using a cell size of  
 227 25 m, 100 m and 200 m respectively. Small cell sizes of 25 m and 50 m (the latter is not  
 228 shown) show nearly indistinguishable, bimodal patterns of events nucleating at  $\sim 15$  km  
 229 depth, suggesting model convergence. A cell size of 100 m leads to a resolution issue  
 230 where periodic behavior is observed, but the bimodal sequence of events is replaced by

231 an alternating sequence of large, small and medium sized events. A cell size of 200 m,  
232 which does not resolve the process zone, reveals a loss of periodic behavior altogether  
233 in favor of a broad range of event sizes and nucleation locations.

## 234 Modeling Groups and Working Platforms

235 For these benchmark exercises, we have used two SCEC-funded workshops (hosted in  
236 April and November 2018, [http://scecddata.usc.edu/cvws/seas/workshop\\_presentations.html](http://scecddata.usc.edu/cvws/seas/workshop_presentations.html))  
237 as open platforms for modelers to share and follow recent scientific progress in the  
238 field, discuss details in benchmark design/results, and collectively decide the directions  
239 of our future efforts, with considerable inputs from students and early career scientists.  
240 Over 10 modeling groups participated in these first two benchmarks; the details of the  
241 group members and different computational methods are summarized in Table . Note  
242 that the modeler name refers to the member of the modeling group who uploaded the  
243 data to the platform for simulations done by the group. It does not necessarily refer to  
244 the code author(s) - see the references in Table for authorship and code availability. For  
245 time-stepping schemes, the majority of groups used adaptive Runge-Kutta methods for  
246 both benchmark problems (the details of which can be found in the references listed in  
247 Table ), with the exception of QDYN, which applies a Bulirsch-Stoer method for BP1,  
248 and BICycle, which incorporates adaptive time-stepping based on stability conditions  
249 derived from the choice of constitutive relationship.

250 To facilitate the submission and comparison of simulation results, we established an  
251 online platform that provides access to community resources and supports the submis-  
252 sion, storage, visualization, and comparison of benchmark results, see Figure 4. For our  
253 first benchmarks, we adopted a platform with similar functionality developed for the  
254 SCEC dynamic rupture simulation group (<http://scecddata.usc.edu/cvws/seas/>).  
255 All modelers can upload and immediately plot time-series data to quickly assess the  
256 overall agreements between models for the time evolution of fault slip, slip rates and  
257 shear stress at representative locations on fault. We use the online platform for prelim-

258 inary model comparisons and analyze more detailed model observables to verify these  
259 computational codes.

## 260 Model Comparisons and What We Learned

261 It is important to note that the problem descriptions for BP1 and BP2 consider a semi-  
262 infinite half-space. Codes based on a volume discretization (FDM/FEM) therefore had  
263 to make their own decisions regarding computational domain truncation and far-field  
264 boundary conditions. The figures in the following sections contain labels generated  
265 by the platform which state the model group name and correspond to results from a  
266 particular model set-up. Some results are followed by the version corresponding to an  
267 alternative set-up, e.g. **abrahams.3** corresponds to results from the **abrahams** group  
268 with an increased computational domain size of  $(L_x, L_z) = (400 \text{ km}, 200 \text{ km})$  and a  
269 remote displacement boundary condition, see the lower right of Figure 4. We discuss  
270 in the next sections the implications that these choices had on model comparisons.

### 271 Results from BP1

272 For the first benchmark problem, BP1, we found qualitative agreements in nucleation  
273 sites, depth extent of rupture, and slip with depth similar to those exemplified by the  
274 slip contours in Figure 3a. In Figure 5 we plot time series of local shear stress and  
275 slip rates at mid-seismogenic depth ( $z = 7.5 \text{ km}$ ) from BP1 over the first 700 years for  
276 different model results. Results from several BEM codes as well as codes with volume  
277 discretization (**abrahams** and **kozdon** modeling groups) and varying computational  
278 domain sizes are compared in Figure 5a-b. The legends indicate the computational  
279 domain size and boundary condition. For BEM codes, HS refers to a half-space, and  
280  $(L_z, \text{boundary condition})$  refers to computational domain depth and boundary condi-  
281 tion, where BC3 corresponds to a periodic boundary condition. For codes with a vol-  
282 ume discretization,  $(L_x/L_z/\text{boundary condition})$ , provides the computational domain  
283 size used and BC1 and BC2 refers to a far-field free surface or a far-field displacement

284 boundary condition, respectively.

285 Figure 5(a-b) show model results from a BEM simulation (**liu**, in black) along with  
286 four model results from volume discretization codes, revealing quantitative differences  
287 in interevent times and peak values. Interevent times for different models range from  
288 approximately 78.3 to 78.8 years over the whole 3000 year simulation period, leading  
289 to model divergence at a near-constant rate. We found that these discrepancies were  
290 caused by choices in domain truncation and boundary conditions. We were surprised to  
291 find that far-field boundary condition type leads to quantitative differences in long-term  
292 fault behavior for relatively small domains (revealed by the blue and orange curves).  
293 This in part is due to small differences in the physical problem being solved by im-  
294 plementations that use periodic or finite domain boundary conditions compared to the  
295 spatial domain BEM methods which represent a truly infinite domain, and therefore  
296 larger loading regions. The green and red curves show how the discrepancy in long-term  
297 behavior among computational methodologies decreases as the physical domain size is  
298 increased, suggesting convergence of results across the modeling groups. Figure 5(c-d)  
299 shows comparisons of all models with  $L_z > 160$  km, further illustrating that excellent  
300 agreements between model results can be achieved with sufficiently large domain sizes.

301 While computational domain size and boundary conditions can lead to model diver-  
302 gence over the long term, the coseismic behavior of individual earthquake are qualita-  
303 tively well reproduced by all models. In Figure 6 we show the time series of shear stress  
304 evolution near the nucleation depth (12.5 km) and slip rate (at a mid-seismogenic depth  
305 of 7.5 km) during the coseismic phase for the 8th event in the sequence from Figure 5.  
306 We chose these plotting depths as they best illustrate model discrepancies, with time  
307 series aligned relative to the rupture initiation time at the depth of 12.5 km. Peak val-  
308 ues in slip rates at 7.5 km depth occur approximately 10s later, and co-seismic surface  
309 reflection phases are marked for all four plots with black arrows. Figures 6(a-b) show  
310 results from models on relatively small computational domains, revealing discrepan-  
311 cies in pre-rupture stress levels near the locked-creeping transition due to differences  
312 in interseismic loading, and resultant coseismic rupture behavior, including peak shear

313 stress and rupture speeds as evidenced by rupture initiation times of the direct and  
314 surface-reflection phases at depth of 7.5 km. Figures 6(c-d) illustrate excellent agree-  
315 ments for model results on larger domains. The discrepancy of  $<1$  MPa in prestress  
316 levels at transitional depths does not result in pronounced difference in fault slip rate  
317 evolution.

## 318 **Results from BP2**

319 For BP2 we suggested submissions of multiple models with different spatial resolutions  
320 from each group, see Table . By design, models with a cell size/node spacing that does  
321 not resolve critical length scales – process zone size and nucleation zone size defined in  
322 (4) and (5) – would produce increased complexity in earthquake sequences, observed  
323 previously (*Rice, 1993; Ben-Zion and Rice, 1997; Day et al., 2005; Lapusta and Liu,*  
324 *2009*), and illustrated in the cumulative slip profiles in Figure 3(b-d).

325 While drastic differences in small event patterns arise for large cell sizes, we found  
326 that with increasing resolution results converge to an alternating sequence of large and  
327 small events among most models. Figure 7a shows the long term evolution of slip rates  
328 at 9.6 km (near the bottom of the seismogenic zone and above the earthquake initiation  
329 depth) for the best model results (with a cell size of 25 m and large computational  
330 domain sizes). We found that even models with similar cell/domain sizes tend to  
331 produce results that are initially closely matching, but diverge over time, likely due to  
332 accumulation of numerical round-off errors and differences in computational techniques.  
333 However, if we zoom in on the tenth event in the sequence (gray bar in Figure 7a), the  
334 time series of fault slip rates, aligned with respect to the start time of seismic slip  
335 at the depth of 12 km within each model, show good agreements (Figure 7b). While  
336 small discrepancies exist in peak slip rates and early source complexity, partly due  
337 to differences in interevent times, the models with the highest resolution exhibit good  
338 agreements in their overall coseismic behavior despite their divergence in the long term.

339 Figure 8 illustrates how model agreement is gradually lost with decreased model  
340 resolution. For cell sizes of 25 m and 50 m, long-term stress evolution near the locked-

341 creeping transition is qualitatively similar for the three models shown and the offset  
 342 in the timing of earthquakes does not significantly affect coseismic behavior of major  
 343 events, as indicated by comparable coseismic stress drops. For large cell sizes of 100 m  
 344 and 200 m, not only is the time offset more random, but also coseismic stress drops and  
 345 event patterns vary between models. Numerical artifacts and different computational  
 346 techniques likely contribute to the divergence of simulation results.

347 In Figure 9 we plot the distribution of earthquake sizes, seismic moment release and  
 348 frequency-size relation for two groups of models (**jiang** and **cattania**) with increasing  
 349 cell sizes. For the 2D problem, we define earthquake size as moment release per length  
 350 for each event,  $M = \int \mu s dz$ , where shear modulus  $\mu = c_s^2 \rho \approx 32$  GPa and  $s$  is total  
 351 coseismic slip over the cell. While better resolved models (cell sizes of 25 m and 50 m)  
 352 show excellent agreements between the two groups, models produce dramatically dif-  
 353 ferent earthquake statistics when cell size increases to 400 m, with the most significant  
 354 discrepancies in smaller earthquakes between the two models (Figure 9a). The distri-  
 355 bution of total seismic moment release,  $M_t$ , calculated as the sum of moment release  
 356 during all earthquakes within a certain magnitude range, also changes with cell sizes,  
 357 though in a similar manner for the two model groups (Figure 9b). Overall, models with  
 358 larger cell sizes tend to produce large earthquakes with reduced total moment; part of  
 359 the moment deficit is accommodated through many more smaller earthquakes and the  
 360 rest through additional aseismic slip. For example, the total moment release through  
 361 largest earthquakes in 400-m models is only half of that in 25-m models. These results  
 362 demonstrate that simulated small earthquakes are especially sensitive to model resolu-  
 363 tion and large earthquake behavior can also be affected. In addition, Figure 9c reveals  
 364 how different simulations with poor resolution can produce similar power-law features  
 365 in frequency-size distributions over certain ranges of earthquake sizes, as a result of  
 366 numerical artifacts rather than well-resolved physics.

367 In Figure 10 we illustrate the effect of model resolution on the partition between  
 368 seismic and aseismic slip. Normalized seismic moment release  $R_s$  is plotted against  
 369 depth for several modeling groups, in solid lines for total seismic moment release and



370 dashed lines for seismic moment due to surface-breaching events.  $R_s = 0$  implies that  
371 all plate motion is accommodated by aseismic slip on the fault, while  $R_s = 1$  means that  
372 all moment is released through earthquakes. A transitional zone in this partitioning  
373 around  $z = H$  and down to  $z = H + h$  ( $H = 15$  and  $h = 3$  in this exercise) is evidenced  
374 in the well-resolved models ( $\Delta_z = 25, 50, 100$  m). The poorly resolved models, however,  
375 illustrate model discrepancies in the seismic/aseismic partitioning, with the near-surface  
376 slip budget being increasingly accommodated by small earthquakes and aseismic slip  
377 with increased cell sizes.

378 In Figure 11 we show interevent times for large surface-breaching events for all  
379 models and cell sizes, showing a strong agreement of  $\sim 110$  years for a cell size of  
380 25 m, with an increasing variability and discrepancies among models with increased cell  
381 size. Although the range of earthquake recurrence intervals are highly dependent on  
382 cell sizes, the median values across models with larger cell sizes do not significantly  
383 deviate from the uniform recurrence intervals in well-resolved models. This suggests  
384 that at least some observables in these models retain information of the true behavior  
385 of physical models and the larger cell sizes can be viewed as a factor that leads to  
386 increased modeling errors.

## 387 Conclusions and Perspectives

388 For the first two SEAS benchmarks we found that discrepancies among well-resolved  
389 models were significantly influenced by computational domain size, with larger do-  
390 mains yielding improvements in agreements, regardless of domain boundary conditions.  
391 Spin-up periods (time required for system to be independent of initial conditions) for  
392 well-resolved models was relatively short - approximately 2-3 events. Results on large  
393 domains agree well initially but still diverge over time, which was not unexpected due  
394 to accumulation of round-off errors and differences in computational techniques. For  
395 BP2 we investigated model resolution and observed qualitative similarities of bimodal  
396 events when the process zone was resolved by approximately 3 and 6 grid points, sug-

397 gesting model convergence. A failure to resolve this length scale however, can lead  
398 to substantial differences in long-term fault behavior as well as earthquake statistics  
399 relevant to seismic hazard, such as frequency-size distributions and interevent times.

400 Although our initial benchmarks have a simple setup, comparison of results for  
401 tens of models have yielded some unexpected and important insights, affirming the  
402 importance of starting simple in a community code verification exercise. The results  
403 and lessons from our initial benchmarks prepare us for future benchmark problems that  
404 incrementally incorporate additional, potentially dominating physical factors, including  
405 fully dynamic ruptures, coupling with fluids, multiple fault segments, nonplanar fault  
406 geometries, and inelastic bulk constitutive behavior (e.g., *Segall and Rice*, 1995; *Noda*  
407 *and Lapusta*, 2010; *Segall and Rice*, 2006; *Segall et al.*, 2010; *Erickson et al.*, 2017;  
408 *Lambert and Barbot*, 2016; *Qiu et al.*, 2016; *Barbot*, 2018; *Ong et al.*, 2019). For future  
409 verification exercises, we plan to address important issues in SEAS simulations, such as  
410 3D effects, heterogeneous fault frictional properties, and full dynamics, which should  
411 advance the state-of-the-art computational capabilities in our field.

412 The goal of the SEAS initiative is to promote advanced models with robust physical  
413 features—a large spectrum of rupture styles and patterns, including slow-slip events,  
414 complex earthquake sequences, fluid effects, dynamic stress changes, and inelastic  
415 deformation—that are currently missing in the large-scale, long-term earthquake sim-  
416 ulator frameworks such as ViscoSim, RSQSIM, Virtual California, and ALLCAL (*Pol-*  
417 *litz*, 2012; *Richards-Dinger and Dieterich*, 2012; *Sachs et al.*, 2012; *Ward*, 2012). This  
418 new generation of verified SEAS models will help determine the controlling physical  
419 mechanisms of earthquake nucleation, propagation, and arrest. The community-wide  
420 initiative would also provide incentives and new ideas to characterize modeling uncer-  
421 tainty for the increasingly complex earthquake source models, an important step in  
422 using physics-based models for the assessment of seismic hazard. Future validation ef-  
423 forts comparing physics-based models with geophysical observations will bridge studies  
424 in paleoseismology, geodesy, and seismology to understand fault behavior over multiple  
425 temporal and spatial scales.

426 **Data and Resources:** Our online platform (<http://scecddata.usc.edu/cvws/seas/>)  
427 is being developed and maintained by M.B. The data for local fault properties are stored  
428 on the platform.

429 **Author Contributions:** B.A.E. and J.J. designed the benchmark problems, analyzed  
430 model results, co-organized the workshops and co-wrote this article. M.B. developed  
431 and maintains the online platform. M.B., N.L., E.M.D. and R.H. provided major  
432 support and advice in forming the working group, obtaining funding, and manuscript  
433 writing. Remaining co-authors provided feedback on benchmark design, participated  
434 in the benchmark exercises, helped revise the manuscript, and are listed alphabetically.

435  
436 **Acknowledgments:** B.A.E., J.J. and M.B. were supported through the Southern Cal-  
437 ifornia Earthquake Center, grant no. 18099 and 19109. Two SEAS-themed workshops  
438 were funded by SCEC awards no. 17151 and 18102. SCEC is funded by NSF Coopera-  
439 tive Agreement EAR-0529922 and USGS Cooperative Agreement 07HQAG0008. This  
440 is SCEC contribution no. 9066.

## References

- Abdelmeguid, M., X. Ma, and A. Elbanna, A novel hybrid finite element-spectral boundary integral scheme for modeling earthquake cycles: Application to rate and state faults with low-velocity zones, *J. Geophys. Res. (to appear)*, doi:10.31223/osf.io/xwhbs, 2019.
- Allison, K., and E. M. Dunham, Earthquake cycle simulations with rate-and-state friction and power-law viscoelasticity, *Tectonophysics*, *733*, 232 – 256, doi:https://doi.org/10.1016/j.tecto.2017.10.021, 2018.
- Ampuero, J.-P., and A. M. Rubin, Earthquake nucleation on rate and state faults – Aging and slip laws, *J. Geophys. Res.-Sol. Ea.*, *113*(B1), doi:10.1029/2007JB005082, 2008.
- Andrews, D. J., Rupture propagation with finite stress in antiplane strain, *J. Geophys. Res.*, *81*, 3575–3582, 1976a.
- Andrews, D. J., Rupture velocity of plane strain shear cracks, *J. Geophys. Res.*, *81*, 5679–5687, 1976b.
- Barall, M., and R. A. Harris, Metrics for comparing dynamic earthquake rupture simulations, *Seismol. Res. Lett.*, *86*(1), doi:10.1785/0220140122, 2015.
- Barbot, S., Asthenosphere flow modulated by megathrust earthquake cycles, *Geophys. Res. Lett.*, *45*, 6018–6031, doi:10.1029/2018GL078197, 2018.
- Barbot, S., Slow-slip, slow earthquakes, period-two cycles, full and partial ruptures, and deterministic chaos in a single asperity fault, *Tectonophysics*, doi:10.1016/j.tecto.2019.228171, 2019.
- Barbot, S., Y. Fialko, and Y. Bock, Postseismic deformation due to the Mw6.0 2004 Parkfield earthquake: Stress-driven creep on a fault with spatially variable rate-and-state friction parameters, *J. Geophys. Res.*, *114*(B07405), doi:10.1029/2008JB005748, 2009.

467 Barbot, S., N. Lapusta, and J.-P. Avouac, Under the hood of the earthquake machine:  
468 Toward predictive modeling of the seismic cycle, *Science*, 336(6082), 707–710, doi:  
469 10.1126/science.1218796, 2012.

470 Ben-Zion, Y., and J. R. Rice, Dynamic simulations of slip on a smooth fault in an elastic  
471 solid, *J. Geophys. Res.-Sol. Ea.*, 102(B8), 17,771–17,784, doi:10.1029/97JB01341,  
472 1997.

473 Bhat, H. S., M. Olives, R. Dmowska, and J. R. Rice, Role of fault branches in earthquake  
474 rupture dynamics, *J. Geophys. Res.*, 112(B11309), 16, doi:10.1029/2007JB005027,  
475 2007.

476 Bradley, A. M., Software for efficient static dislocation–traction calculations in fault  
477 simulators, *Seismol. Res. Lett.*, 85(6), 1358–1365, doi:10.1785/0220140092, 2014.

478 Cattania, C., Complex earthquake behavior on simple faults, *submitted to Geophys.*  
479 *Res. Lett.*, doi:10.31223/osf.io/hgbjx, 2019.

480 Chen, T., and N. Lapusta, Scaling of small repeating earthquakes explained by inter-  
481 action of seismic and aseismic slip in a rate and state fault model, *J. Geophys. Res.*,  
482 114(B01311), doi:10.1029/2008JB005749, 2009.

483 Day, S. M., Three-dimensional finite difference simulation of fault dynamics: rectan-  
484 gular faults with fixed rupture velocity, *Bull. Seismol. Soc. Am.*, 72(3), 705–727,  
485 1982.

486 Day, S. M., L. A. Dalguer, N. Lapusta, and Y. Liu, Comparison of finite difference and  
487 boundary integral solutions to three-dimensional spontaneous rupture, *J. Geophys.*  
488 *Res.-Sol. Ea.*, 110(B12), doi:10.1029/2005JB003813, 2005.

489 Dieterich, J. H., Modeling of rock friction: 1. experimental results and constitutive equa-  
490 tions, *J. Geophys. Res.-Sol. Ea.*, 84(B5), 2161–2168, doi:10.1029/JB084iB05p02161,  
491 1979.

492 Dieterich, J. H., K. B. Richards-Dinger, and K. A. Kroll, Modeling injection-induced  
493 seismicity with the physics-based earthquake simulator RSQSim, *Seismol. Res. Lett.*,  
494 86(4), doi:10.1785/0220150057, 2015.

495 Duan, B., and D. D. Oglesby, Heterogeneous fault stresses from previous earthquakes  
496 and the effect on dynamics of parallel strike-slip faults, *J. Geophys. Res.*, 111(B5),  
497 2006.

498 Dublanchet, P., The dynamics of earthquake precursors controlled by effective friction,  
499 *Geophys. J. Int.*, 212(2), 853–871, 2017.

500 Dublanchet, P., P. Bernard, and P. Favreau, Interactions and triggering in a 3-d rate-  
501 and-state asperity model, *J. Geophys. Res.*, 118(5), 2225–2245, 2013.

502 Dunham, E. M., D. Belanger, L. Cong, and J. E. Kozdon, Earthquake ruptures with  
503 strongly rate-weakening friction and off-fault plasticity, Part:1: Planar faults, *Bull.*  
504 *Seismol. Soc. Am.*, 101(5), 2296–2307, doi:10.1785/0120100075, 2011a.

505 Dunham, E. M., D. Belanger, L. Cong, and J. E. Kozdon, Earthquake ruptures with  
506 strongly rate-weakening friction and off-fault plasticity, Part:2: Nonplanar faults,  
507 *Bull. Seismol. Soc. Am.*, 101(5), 2308–2322, doi:10.1785/0120100076, 2011b.

508 Erickson, B. A., and E. M. Dunham, An efficient numerical method for earthquake  
509 cycles in heterogeneous media: Alternating subbasin and surface-rupturing events on  
510 faults crossing a sedimentary basin, *J. Geophys. Res.-Sol. Ea.*, 119(4), 3290–3316,  
511 doi:10.1002/2013JB010614, 2014.

512 Erickson, B. A., E. M. Dunham, and A. Khosravifar, A finite difference method for  
513 off-fault plasticity throughout the earthquake cycle, *J. Mech. Phys. Solids*, 109, 50 –  
514 77, doi:10.1016/j.jmps.2017.08.002, 2017.

515 Floyd, M. A., et al., Spatial variations in fault friction related to lithology from rupture  
516 and afterslip of the 2014 South Napa, California, earthquake, *Geophys. Res. Lett.*,  
517 43(13), 6808–6816, doi:10.1002/2016GL069428, 2016.

518 Gabriel, A.-A., J.-P. Ampuero, L. A. Dalguer, and P. M. Mai, The transition of dynamic  
519 rupture styles in elastic media under velocity-weakening friction, *J. Geophys. Res.*,  
520 *117*(B9), 2012.

521 Goswami, A., and S. Barbot, Slow-slip events in semi-brittle serpentinite fault zones,  
522 *Scientific reports*, *8*(1), 6181, 2018.

523 Harris, R. A., et al., The SCEC/USGS dynamic earthquake rupture code verification  
524 exercise, *Seismol. Res. Lett.*, *80*, 119–126, doi:10.1785/gssrl.80.1.119, 2009.

525 Harris, R. A., et al., A suite of exercises for verifying dynamic earthquake rupture codes,  
526 *Seismol. Res. Lett.*, *89*(3), doi:https://doi.org/10.1785/0220170222, 2018.

527 Hori, T., N. Kato, K. Hirahara, T. Baba, and Y. Kaneda, A numerical simulation of  
528 earthquake cycles along the Nankai Trough in southwest Japan: Lateral variation in  
529 frictional property due to the slab geometry controls the nucleation position, *Earth  
530 Planet Sc. Lett.*, *228*(3-4), 215–226, 2004.

531 Jiang, J., and Y. Fialko, Reconciling seismicity and geodetic locking depths on the  
532 Anza section of the San Jacinto fault, *Geophys. Res. Lett.*, *43*(20), 10,663–10,671,  
533 doi:10.1002/2016GL071113, 2016.

534 Jiang, J., and N. Lapusta, Deeper penetration of large earthquakes on seismically qui-  
535 escent faults, *Science*, *352*(6291), 1293–1297, doi:10.1126/science.aaf1496, 2016.

536 Johnson, K. M., R. Bürgmann, and K. Larson, Frictional properties of the San Andreas  
537 Fault near Parkfield, California, inferred from models of afterslip following the 2004  
538 earthquake, *Bull. Seismol. Soc. Am.*, *96*(4B), doi:10.1785/0120050808, 2006.

539 Kaneko, Y., J.-P. Avouac, and N. Lapusta, Towards inferring earthquake patterns from  
540 geodetic observations of interseismic coupling, *Nat. Geosci.*, *3*, 2010.

541 Kaneko, Y., J.-P. Ampuero, and N. Lapusta, Spectral-element simulations of long-term  
542 fault slip: Effect of low-rigidity layers on earthquake-cycle dynamics, *J. Geophys.  
543 Res.-Sol. Ea.*, *116*(B10), doi:10.1029/2011JB008395, 2011.

544 Kato, N., Seismic cycle on a strike-slip fault with rate-and state-dependent strength  
545 in an elastic layer overlying a viscoelastic half-space, *Earth Planets Space*, 54(11),  
546 1077–1083, 2002.

547 Kato, N., Deterministic chaos in a simulated sequence of slip events on a single isolated  
548 asperity, *Geophys. J. Int.*, 198(2), 727–736, 2014.

549 Kato, N., Earthquake cycles in a model of interacting fault patches: Complex behavior  
550 at transition from seismic to aseismic slip, *Bull. Seismol. Soc. Am.*, 106(4), 1772–  
551 1787, 2016.

552 Kozdon, J. E., and E. M. Dunham, Rupture to the trench: Dynamic rupture simulations  
553 of the 11 March 2011 Tohoku earthquake, *Bull. Seismol. Soc. Am.*, 103(2B), 1275–  
554 1289, doi:10.1785/0120120136, 2013.

555 Lambert, V., and S. Barbot, Contribution of viscoelastic flow in earthquake cycles  
556 within the lithosphere-asthenosphere system, *Geophys. Res. Lett.*, 43(19), 142–154,  
557 2016.

558 Lapusta, N., and Y. Liu, Three-dimensional boundary integral modeling of spontaneous  
559 earthquake sequences and aseismic slip, *J. Geophys. Res.-Sol. Ea.*, 114(B9), doi:  
560 10.1029/2008JB005934, 2009.

561 Lapusta, N., and J. R. Rice, Nucleation and early seismic propagation of small and  
562 large events in a crustal earthquake model, *J. Geophys. Res.*, 108(B4, 2205), 2003.

563 Lapusta, N., J. R. Rice, Y. Ben-Zion, and G. Zheng, Elastodynamic analysis for slow  
564 tectonic loading with spontaneous rupture episodes on faults with rate- and state-  
565 dependent friction, *J. Geophys. Res.-Sol. Ea.*, 105(B10), 23,765–23,789, doi:10.1029/  
566 2000JB900250, 2000.

567 Li, D., and Y. Liu, Spatiotemporal evolution of slow slip events in a nonplanar fault  
568 model for northern Cascadia subduction zone, *J. Geophys. Res.*, 121(9), 6828–6845,  
569 2016.



570 Li, D., and Y. Liu, Modeling slow-slip segmentation in Cascadia subduction zone con-  
571 strained by tremor locations and gravity anomalies, *J. Geophys. Res.*, *122*(4), 3138–  
572 3157, 2017.

573 Liu, Y., Numerical simulations on megathrust rupture stabilized under strong dilatancy  
574 strengthening in slow slip region, *Geophys. Res. Lett.*, *40*(7), 1311–1316, doi:10.1002/  
575 grl.50298, 2013.

576 Liu, Y., and J. R. Rice, Aseismic slip transients emerge spontaneously in three-  
577 dimensional rate and state modeling of subduction earthquake sequences, *J. Geophys.*  
578 *Res.*, *110*(B08307), doi:10.1029/2004JB003424, 2005.

579 Liu, Y., and J. R. Rice, Spontaneous and triggered aseismic deformation transients in a  
580 subduction fault model, *J. Geophys. Res.*, *112*(B09404), doi:10.1029/2007JB004930,  
581 2007.

582 Lozos, J. C., D. D. Oglesby, B. Duan, and S. G. Wesnousky, The effects of double fault  
583 bends on rupture propagation: A geometrical parameter study, *Bull. Seismol. Soc.*  
584 *Am.*, *101*(1), 385–398, 2011.

585 Luo, Y., and J. P. Ampuero, Numerical simulation of tremor migration triggered by  
586 slow slip and rapid tremor reversals, *AGU Fall Meeting Abstracts*, S33C-02, 2011.

587 Luo, Y., and J. P. Ampuero, Preprint: Tremor migration patterns and the collective  
588 behavior of deep asperities mediated by creep, doi:10.31223/osf.io/mbcav, 2017.

589 Ma, X., and A. Elbanna, Dynamic rupture propagation on fault planes with explicit  
590 representation of short branches, *Earth Planet Sc. Lett.*, *523*, 115,702, doi:10.1016/j.  
591 epsl.2019.07.005, 2019.

592 Marone, C., Laboratory-derived friction laws and their application to seismic faulting,  
593 *Ann. Rev. Earth Pl. Sc.*, *26*(1), 643–696, doi:10.1146/annurev.earth.26.1.643, 1998.

594 McClure, M. W., and R. N. Horne, Investigation of injection-induced seismicity using a  
595 coupled fluid flow and rate/state friction model, *Geophysics*, 76(6), WC181–WC198,  
596 doi:10.1190/geo2011-0064.1, 2011.

597 Mckay, M. B., B. A. Erickson, and J. E. Kozdon, A computational method for earth-  
598 quake cycles within anisotropic media, *Geophys. J. Int.*, doi:10.1093/gji/ggz320,  
599 2019.

600 Meade, B. J., Y. Klinger, and E. A. Hetland, Inference of multiple earthquake-cycle  
601 relaxation timescales from irregular geodetic sampling of interseismic deformation,  
602 *Bull. Seismol. Soc. Am.*, 103(5), 2824–2835, doi:10.1785/0120130006, 2013.

603 Mele Veedu, M., and S. Barbot, The Parkfield tremors reveal slow and fast ruptures on  
604 the same asperity, *Nature*, 532(7599), 361–365, doi:10.1038/nature17190, 2016.

605 Michel, S., J.-P. Avouac, N. Lapusta, and J. Jiang, Pulse-like partial ruptures and high-  
606 frequency radiation at creeping-locked transition during megathrust earthquakes,  
607 *Geophys. Res. Lett.*, 44(16), 8345–8351, doi:10.1002/2017GL074725, 2017.

608 Mitsui, Y., and K. Hirahara, Fault instability on a finite and planar fault related to  
609 early phase of nucleation, *J. Geophys. Res.*, 116(B6), 2011.

610 Nakata, R., M. Hyodo, and T. Hori, Numerical simulation of afterslips and slow slip  
611 events that occurred in the same area in Hyuga-nada of southwest Japan, *Geophys.*  
612 *J. Int.*, 190(2), 1213–1220, doi:10.1111/j.1365-246X.2012.05552.x, 2012.

613 Nielsen, S. B., J. Carlson, and K. B. Olsen, Influence of friction and fault geometry on  
614 earthquake rupture, *J. Geophys. Res.*, 105(B3), 6069–6088, 2000.

615 Noda, H., and N. Lapusta, Three-dimensional earthquake sequence simulations with  
616 evolving temperature and pore pressure due to shear heating: Effect of heterogeneous  
617 hydraulic diffusivity, *J. Geophys. Res.*, 115(B12314), doi:10.1029/2010JB007780,  
618 2010.

619 Noda, H., and N. Lapusta, Stable creeping fault segments can become destructive as a  
620 result of dynamic weakening, *Nature*, 493(7433), 518–521, 2013.

621 Ohtani, M., and K. Hirahara, Effect of the Earth’s surface topography on quasi-dynamic  
622 earthquake cycles, *Geophys. J. Int.*, 203(1), 384–398, doi:10.1093/gji/ggv187, 2015.

623 Olsen, K. B., R. Madariaga, and R. J. Archuleta, Three-dimensional dynamic simulation  
624 of the 1992 Landers earthquake, *Science*, 278(5339), 834–838, 1997.

625 Ong, M., Su Qing, S. Barbot, and J. Hubbard, Physics-based scenario of earthquake  
626 cycles on the Ventura thrust system, California: The effect of variable friction and  
627 fault geometry, *J. Pure Appl. Geophys.*, doi:10.1007/s00024-019-02111-9, 2019.

628 Palmer, A. C., and J. R. Rice, The growth of slip surfaces in the progressive failure of  
629 over-consolidated clay, *Proc. Roy. Soc. Lond. A*, 332(1591), 527–548, doi:10.1098/  
630 rspa.1973.0040, 1973.

631 Perfettini, H., and J.-P. Ampuero, Dynamics of a velocity strengthening fault region:  
632 Implications for slow earthquakes and postseismic slip, *J. Geophys. Res.-Sol. Ea.*,  
633 113(B9), doi:10.1029/2007JB005398, 2008.

634 Perfettini, H., and J.-P. Avouac, Postseismic relaxation driven by brittle creep: A possi-  
635 ble mechanism to reconcile geodetic measurements and the decay rate of aftershocks,  
636 application to the Chi-Chi earthquake, Taiwan, *J. Geophys. Res.*, 109(B02304), 2004.

637 Perfettini, H., and J.-P. Avouac, Modeling afterslip and aftershocks following the 1992  
638 Landers earthquake, *J. Geophys. Res.*, 112(B07409), 2007.

639 Pollitz, F. F., ViscoSim Earthquake Simulator , *Seismol. Res. Lett.*, 83(6), 979–982,  
640 doi:10.1785/0220120050, 2012.

641 Qiu, Q., et al., The mechanism of partial rupture of a locked megathrust: The role of  
642 fault morphology, *Geology*, 44(10), 875–878, doi:10.1130/G38178.1, 2016.

643 Rice, J. R., Spatio-temporal complexity of slip on a fault, *J. Geophys. Res.*, *98*(B6),  
644 9885–9907, 1993.

645 Rice, J. R., and S. T. Tse, Dynamic motion of a single degree of freedom system following  
646 a rate and state dependent friction law, *J. Geophys. Res.*, *91*(B1), 521–530, 1986.

647 Richards-Dinger, K., and J. H. Dieterich, RSQSim earthquake simulator, *Bull. Seismol.*  
648 *Soc. Am.*, *83*(6), 983–990, doi:<https://doi.org/10.1785/0220120105>, 2012.

649 Ripperger, J., J.-P. Ampuero, P. M. Mai, and D. Giardini, Earthquake source charac-  
650 teristics from dynamic rupture with constrained stochastic fault stress, *J. Geophys.*  
651 *Res.-Sol. Ea.*, *112*(B4), doi:10.1029/2006JB004515, 2007.

652 Rubin, A. M., and J.-P. Ampuero, Earthquake nucleation on (aging) rate and state  
653 faults, *J. Geophys. Res.-Sol. Ea.*, *110*(B11), doi:10.1029/2005JB003686, 2005.

654 Ruina, A., Slip instability and state variable friction laws, *J. Geophys. Res.-Sol. Ea.*,  
655 *88*(B12), 10,359–10,370, doi:10.1029/JB088iB12p10359, 1983.

656 Sachs, M. K., E. M. Heien, D. L. Turcotte, M. B. Yikilmaz, J. B. Rundle, and L. H.  
657 Kellogg, Virtual California Earthquake Simulator, *Seismol. Res. Lett.*, *83*(6), 973–  
658 978, doi:10.1785/0220120052, 2012.

659 Segall, P., and A. M. Bradley, The role of thermal pressurization and dilatancy in  
660 controlling the rate of fault slip, *J. Appl. Mech.*, *79*(3), doi:10.1115/1.4005896, 2012a.

661 Segall, P., and A. M. Bradley, Slow-slip evolves into megathrust earthquakes in 2d nu-  
662 merical simulations, *Geophys. Res. Lett.*, *39*(18), doi:10.1029/2012GL052811, 2012b.

663 Segall, P., and J. R. Rice, Dilatancy, compaction, and slip instability of a fluid infiltrated  
664 fault, *J. Geophys. Res.*, *100*, 22,155–22,171, 1995.

665 Segall, P., and J. R. Rice, Does shear heating of pore fluid contribute to earthquake  
666 nucleation?, *J. Geophys. Res.*, *111*(B09316), 17, 2006.

667 Segall, P., A. M. Rubin, A. M. Bradley, and J. R. Rice, Dilatant strengthening as a  
668 mechanism for slow slip events, *J. Geophys. Res.*, 115(B12305), 2010.

669 Shi, Z., and S. M. Day, Rupture dynamics and ground motion from 3-d rough-fault  
670 simulations, *J. Geophys. Res.-Sol. Ea.*, 118(3), 1122–1141, doi:10.1002/jgrb.50094,  
671 2013.

672 Tse, S. T., and J. R. Rice, Crustal earthquake instability in relation to the depth  
673 variation of frictional slip properties, *J. Geophys. Res.*, 91(B9), 9452–9472, 1986.

674 Tullis, T. E., et al., Generic earthquake simulator, *Seismol. Res. Lett.*, 83, 959–963,  
675 doi:10.1785/0220120093, 2012.

676 van Dinther, Y., T. V. Gerya, L. A. Dalguer, F. Corbi, F. Funiciello, and P. M. Mai,  
677 The seismic cycle at subduction thrusts: 2. dynamic implications of geodynamic  
678 simulations validated with laboratory models, *J. Geophys. Res.-Sol. Ea.*, 118(4),  
679 1502–1525, doi:10.1029/2012JB009479, 2013.

680 Viesca, R. C., Stable and unstable development of an interfacial sliding instability,  
681 *Phys. Rev. E*, 93, 060,202, doi:10.1103/PhysRevE.93.060202, 2016a.

682 Viesca, R. C., Self-similar slip instability on interfaces with rate- and state-dependent  
683 friction, *Proceedings of the Royal Society A: Mathematical, Physical and Engineering*  
684 *Sciences*, 472(2192), 20160,254, doi:10.1098/rspa.2016.0254, 2016b.

685 Ward, S. N., ALLCAL Earthquake Simulator, *Seismol. Res. Lett.*, 83(6), 964–972,  
686 doi:10.1785/0220120056, 2012.

687 Wei, M., Y. Kaneko, Y. Liu, and J. J. McGuire, Episodic fault creep events in California  
688 controlled by shallow frictional heterogeneity, *Nat. Geosci.*, 6, 566–570, doi:10.1038/  
689 ngeo1835, 2013.

690 Wei, M., Y. Kaneko, P. Shi, and Y. Liu, Numerical modeling of dynamically triggered  
691 shallow slow slip events in New Zealand by the 2016 Mw 7.8 Kaikoura earthquake,  
692 *Geophys. Res. Lett.*, 45(10), 4764–4772, 2018.

- 693 Wollherr, S., A.-A. Gabriel, and P. M. Mai, Landers 1992 "reloaded": Integrative  
694 dynamic earthquake rupture modeling, *J. Geophys. Res.-Sol. Ea.*, 2018.
- 695 Wu, Y., and X. Chen, The scale-dependent slip pattern for a uniform fault model  
696 obeying the rate-and state-dependent friction law, *J. Geophys. Res.*, 119(6), 4890–  
697 4906, 2014.
- 698 Xu, J., H. Zhang, and X. Chen, Rupture phase diagrams for a planar fault in 3-d  
699 full-space and half-space, *Geophys. J. Int.*, 202(3), 2194–2206, 2015.

Table 1: Parameter values used in the benchmark problem

Parameter	Definition	Value, Units
$\rho$	density	2670 kg/m <sup>3</sup>
$c_s$	shear wave speed	3.464 km/s
$\sigma_n$	effective normal stress on fault	50 MPa
$a$	rate-and-state parameter	variable (see Fig. 1)
$b$	rate-and-state parameter	variable (see Fig. 1)
$L$	critical slip distance	BP1: 0.008 m BP2: 0.004 m
$V_p$	plate rate	10 <sup>-9</sup> m/s
$V_{\text{init}}$	initial slip rate	10 <sup>-9</sup> m/s
$V_0$	reference slip rate	10 <sup>-6</sup> m/s
$f_0$	reference friction coefficient	0.6
$H$	depth extent of uniform VW region	15 km
$h$	width of VW-VS transition zone	3 km
$W_f$	width of rate-and-state fault	40 km
$\Delta z$	suggested cell sizes	BP1: 25 m BP2: 25 m, 50 m, 100 m, 200 m, 300 m, 400 m, 800 m
$t_f$	final simulation time	BP1: 3000 years BP2: 1200 years
$L_z$	depth of computational domain	<i>not specified</i>
$L_x$	off-fault distance of computational domain	<i>not specified</i>

Table 2: Details of participating SEAS codes and modeling groups.

<b>Code Name</b>	<b>Type</b>	<b>Modeler Name &amp; Group Members</b>	<b>References</b>
SCycle	FDM	<b>abrahams</b> (Abrahams/ Allison/Dunham)	<i>Erickson and Dunham (2014)</i> <i>Allison and Dunham (2018)</i> <a href="https://github.com/kali-allison/SCycle">https://github.com/kali-allison/SCycle</a>
FDCycle	FDM	<b>erickson</b> (Erickson/Mckay)	<i>Erickson and Dunham (2014)</i> <a href="https://github.com/brittany-erickson/FDCycle">https://github.com/brittany-erickson/FDCycle</a>
QDESDG	DG-FEM	<b>kozdon</b> (Kozdon)	<a href="https://github.com/jkozdon/QDESDG">https://github.com/jkozdon/QDESDG</a>
Unicycle	BEM	<b>barbot</b> (Barbot)	<i>Barbot (2019)</i> <a href="http://bitbucket.org/sbarbot">http://bitbucket.org/sbarbot</a>
FDRA	BEM	<b>cattania</b> (Cattania/Segall)	<i>Segall and Bradley (2012b); Bradley (2014)</i>
BICycle	BEM	<b>jiang</b> (Jiang) <b>lambert</b> (Lambert/Lapusta) <b>xma</b> (Ma/Elbanna)	<i>Lapusta et al. (2000); Lapusta and Liu (2009)</i>
QDYN	BEM	<b>luo</b> (Luo/Idini/ van den Ende/Ampuero)	<i>Luo and Ampuero (2017)</i> <a href="https://github.com/ydluo/qdyn">https://github.com/ydluo/qdyn</a>
ESAM	BEM	<b>liu</b> (Liu) <b>wei</b> (Wei/Shi)	<i>Liu and Rice (2007)</i>



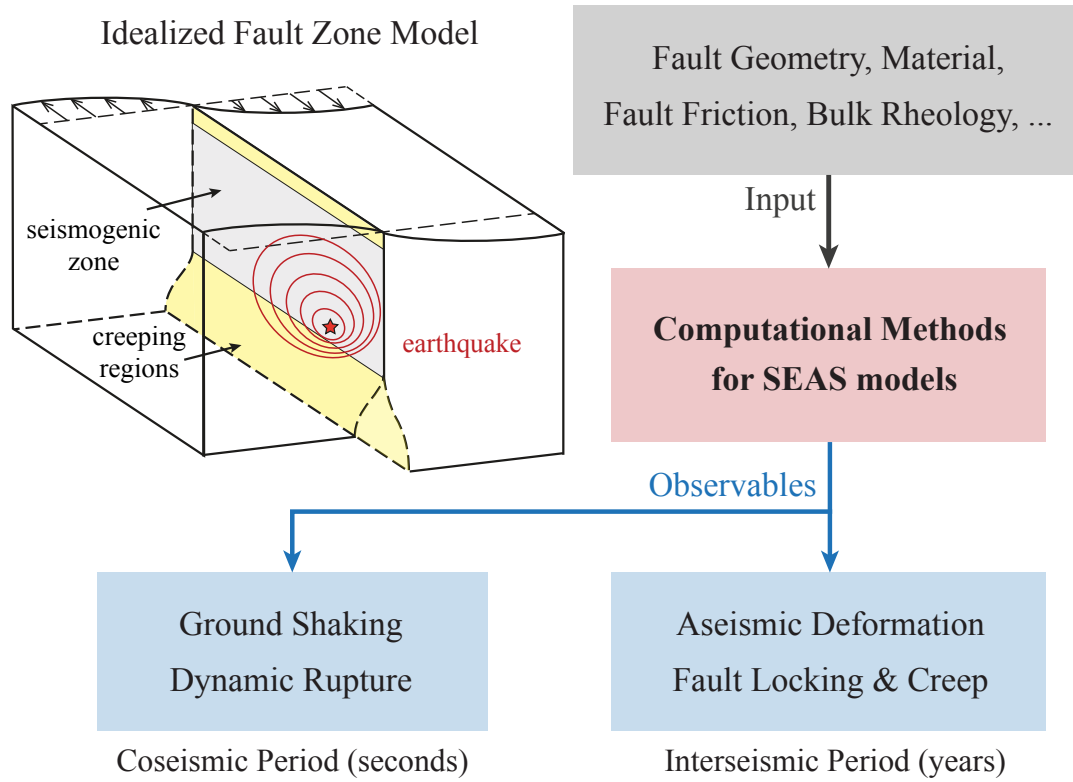


Figure 1: Ingredients and observables for SEAS (sequences of earthquakes and aseismic slip) models. In a conceptual fault-zone model, earthquakes initiate at seismogenic depths (red star) and rupture through the interseismically locked regions (gray), while aseismic slip occurs in deeper and sometimes shallower regions (yellow). For numerical models, given fault zone properties, computational simulations can reproduce long-term fault locking and creep over years to decades, punctuated by dynamic earthquake ruptures over seconds to minutes. Seismic shaking and aseismic deformation are typical observables from the surface.

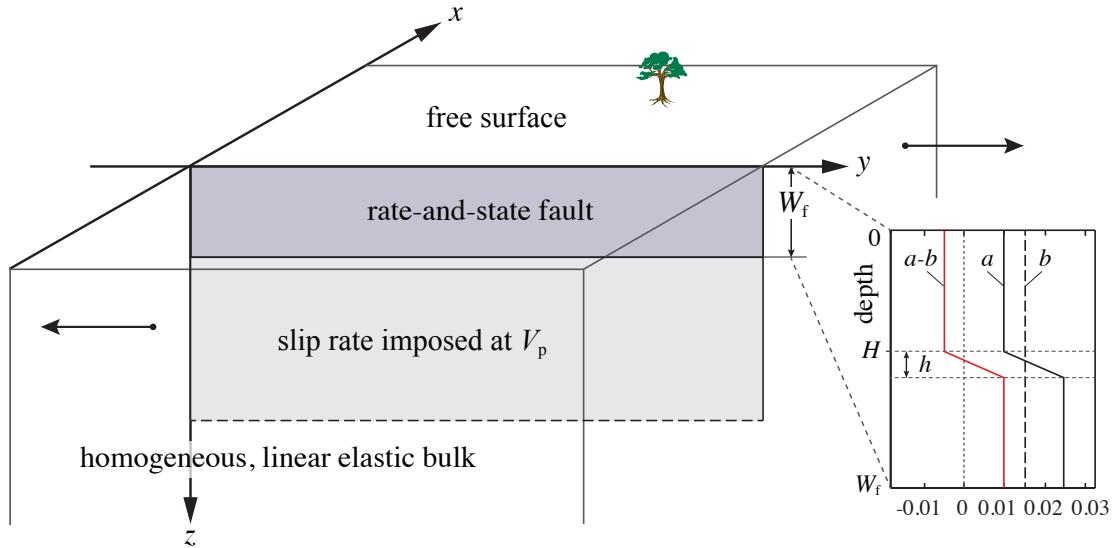


Figure 2: Our first SEAS benchmark is based on the model in *Rice (1993)*, where a planar fault is embedded in a homogeneous, linear elastic half-space with a free surface. A vertical cross-section of the 3D setting is taken so that slip varies only with depth and deformation is 2D antiplane strain. The fault is governed by rate-and-state friction with depth-dependent frictional parameters  $a$  and  $b$  above the depth  $W_f$ , below which a steady slow loading rate  $V_p$  is assumed. The friction-controlled fault is seismogenic due to velocity-weakening properties ( $(a - b) < 0$ ) down to depth  $H$  and accommodates aseismic creep at greater depths due to velocity-strengthening properties ( $(a - b) > 0$ ). Earthquakes nucleate spontaneously, with inertia approximated with radiation damping.

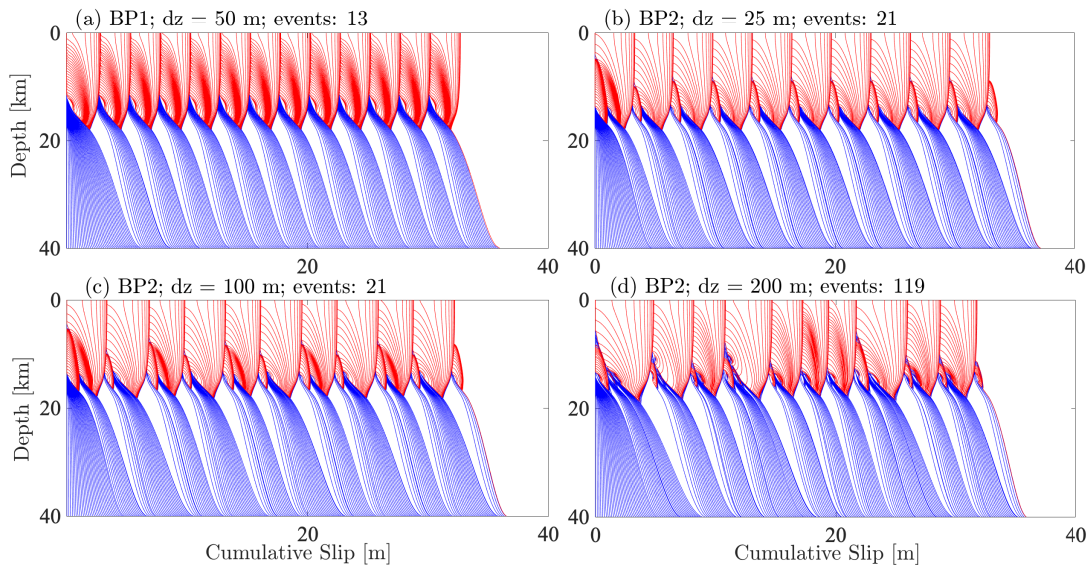
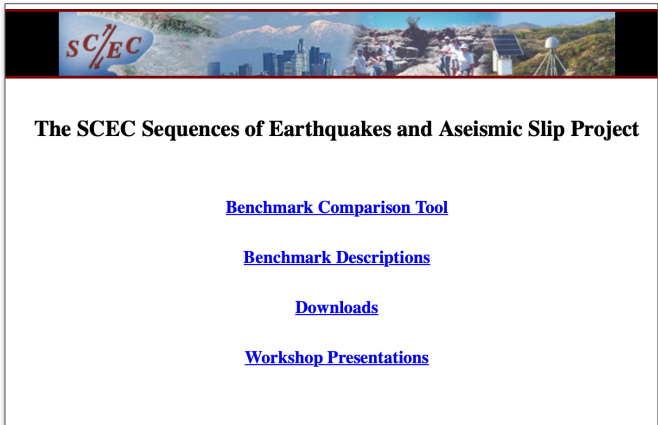


Figure 3: Cumulative slip profiles plotted over a 1,200 year period in blue every 5 years during interseismic loading and in red every second during quasi-dynamic rupture. Results were obtained using the BICyclE code for (a) BP1 with a cell size of 50 m, (b) BP2 with a cell size of 25 m, (c) BP2 with a cell size of 100 m and (d) BP2 with a cell size of 200 m. Number of events also listed, where we define a seismic event to be one with a local slip rate  $> 0.01$  m/s separated by aseismic periods of at least 15 s.



**The SCEC Sequences of Earthquakes and Aseismic Slip Project**

[Benchmark Comparison Tool](#)

[Benchmark Descriptions](#)

[Downloads](#)

[Workshop Presentations](#)

Benchmarks			
Name	Date	Description	Action
bp1	4/14/2018 8:08 AM	2D Antiplane Shear	Select
bp2	10/6/2018 6:20 AM	2D Antiplane Shear, Varying Cell Size	Select

Users			
		Select Checked	Select All
Name	Description		
<input type="checkbox"/>	abrahams	100 km X 80 km: Free surface outer BC	Select
<input type="checkbox"/>	abrahams.2	100 km X 80 km: Vp/2 outer BC	Select
<input type="checkbox"/>	abrahams.3	400 km X 200 km: Vp/2 outer BC	Select
<input type="checkbox"/>	barbot	Sylvain Barbot (Fortran90)	Select
<input type="checkbox"/>	barbot.2	Sylvain Barbot (Matlab)	Select
<input type="checkbox"/>	cattania	Camilla Cattania - fdra (bem)	Select
<input type="checkbox"/>	cattania.2	Camilla Cattania - fdra (fft, 160 km)	Select
<input type="checkbox"/>	cattania.3	Camilla Cattania - fdra (fft, 640 km)	Select
<input type="checkbox"/>	erickson	Brittany Erickson	Select
<input type="checkbox"/>	erickson.2	Brittany Erickson	Select

Figure 4: Online platform for the SEAS working group. (Left) Home page for our website. (Top right) Currently available benchmarks. (Bottom right) Examples of BP1 model submissions.

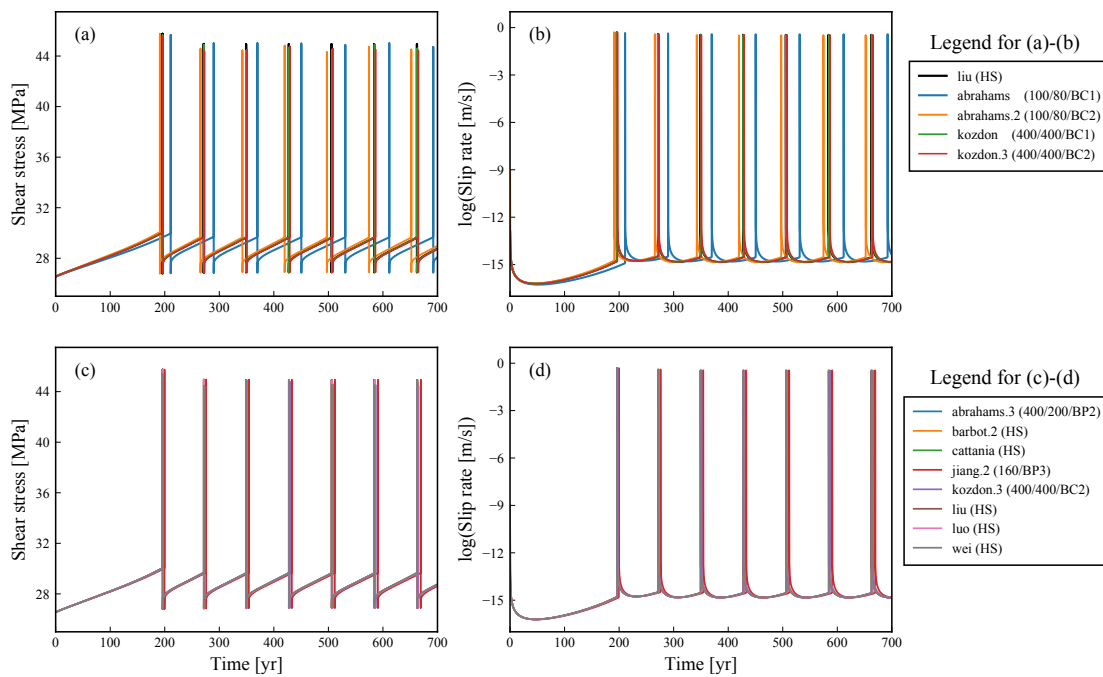


Figure 5: Long-term behavior of BP1 models. (a) Shear stress and (b) slip rates at the depth of 7.5 km in models with different outer boundary conditions (BC) and computational domain sizes. (c) Shear stress and (d) slip rates at depth of 7.5 km in models with sufficiently large computational domain sizes. Legend labels indicate model names followed by information on BC and domain size, namely,  $(L_x/L_z/BC)$  for FDM/FEM, and  $(L_z/BC)$  or (HS, half-space) for BEM. BC1 and BC2 refer to the far-field free surface or displacement BC and BC3 refers to the periodic BC.

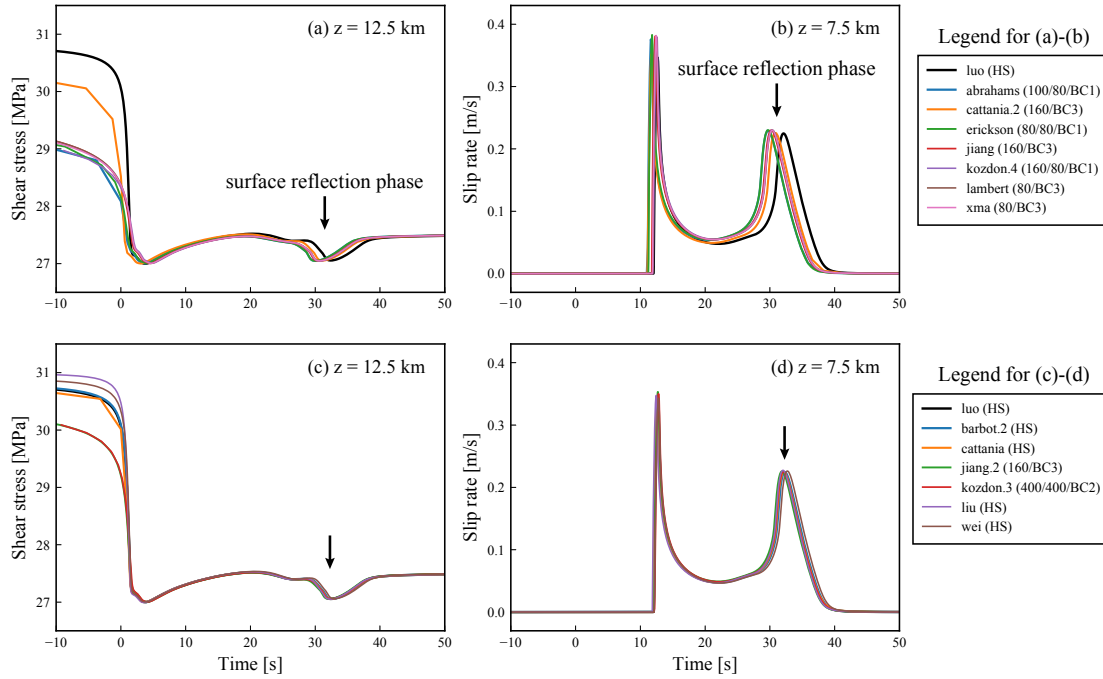


Figure 6: Coseismic behavior of BP1 models. Coseismic phase during the 8th event in Figure 5 is shown. Models with smaller computational domain sizes show discrepancies in (a) shear stresses at 12.5km depth and (b) slip rates at 7.5km depth. Models with sufficiently large computational domain sizes are compared for (c) shear stresses at 12.5km depth and (d) slip rates at 7.5km depth. Time series are aligned relative to the rupture initiation time at the depth of 12.5 km in each model. Note that the half-space solution **luo** is the same in (b) and (d) and serves as a reference. The surface reflection phase is marked by a black arrow.

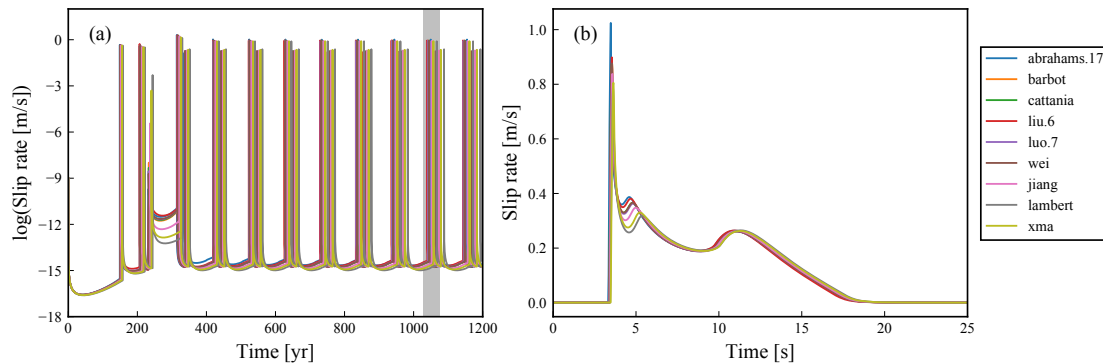


Figure 7: Comparison of best-resolved BP2 models (cell size of  $\sim 25$  m). (a) Long-term evolution of slip rates at depth of 9.6 km; (b) coseismic evolution of slip rates at the depth of 9.6 km for the 10th large events in the sequence (marked in gray in (a)). Time series are aligned relative to the rupture initiation time at the depth of 12 km in each model.

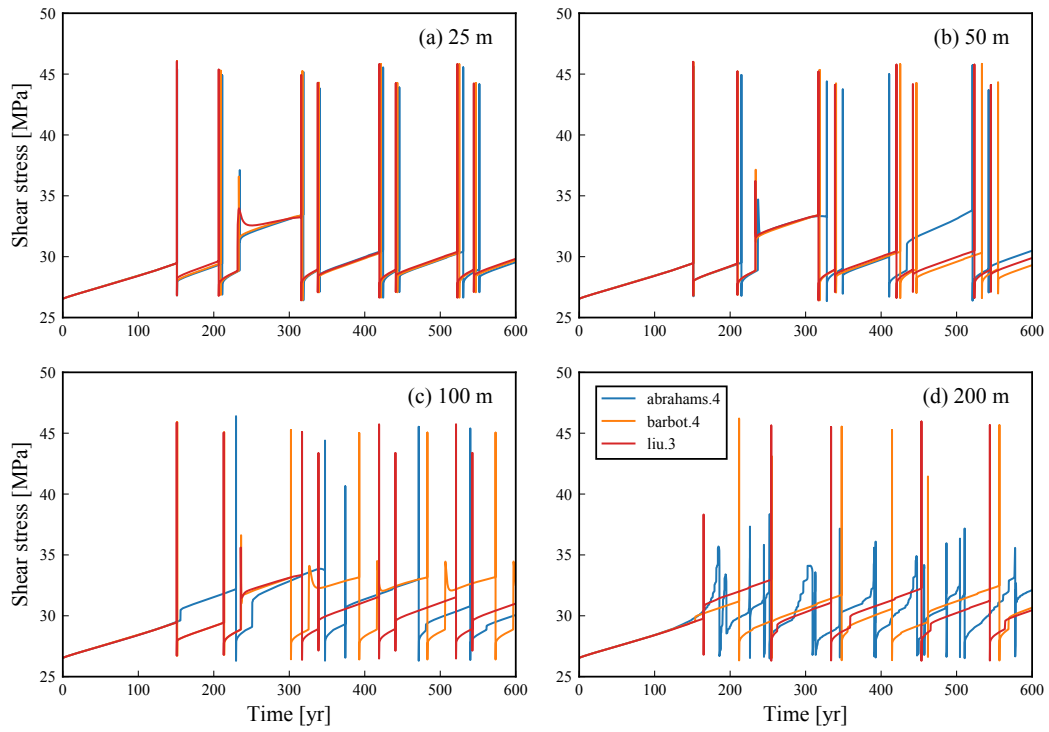


Figure 8: Increasing discrepancy in BP2 models due to an increased cell size of (a) 25 m, (b) 50 m, (c) 100 m, and (d) 200 m. Time evolution of shear stress at the depth of 9.6 km during the first 600 years is shown for models from three groups (**abrahams**, **barbot**, and **liu**).

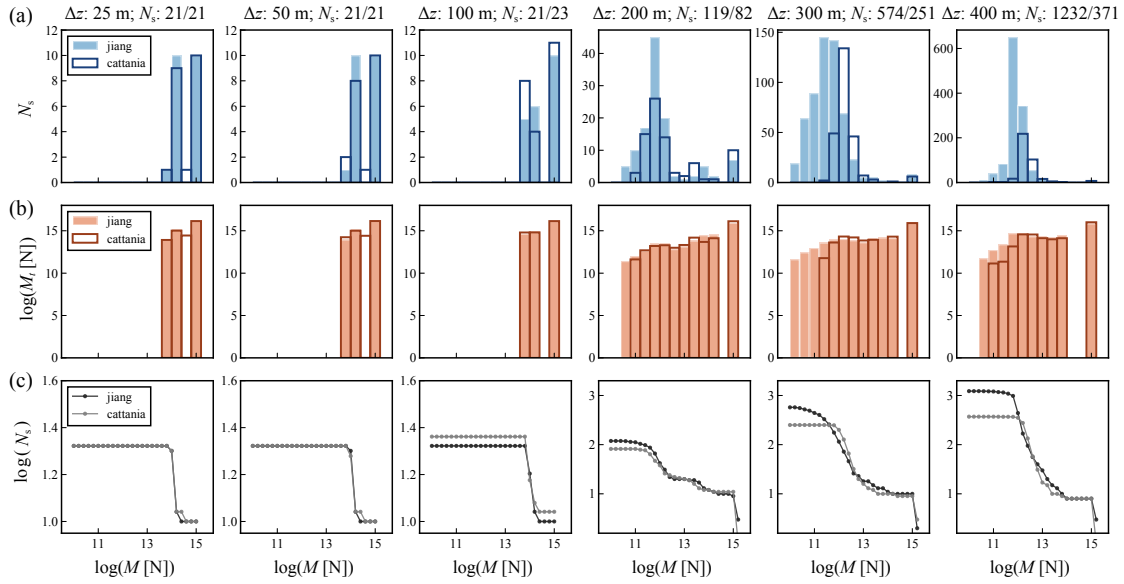


Figure 9: Effect of model resolution on earthquake patterns. Distribution of (a, top row) earthquake sizes and (b, middle row) of total seismic moment release per unit length,  $M$  (in unit of  $N$ ) and (c, bottom row) frequency-size relation. Models from two groups (**jiang** and **cattania**) are compared. The corresponding cell size ( $\Delta z$ ) and total seismic event numbers ( $N_s$ ) are marked in the titles. Seismic moment  $M$  refers to the seismic moment of each earthquake; total seismic moment  $M_t$  refers to the sum of moment release for all earthquakes within each magnitude bin.  $N_s$  in (c) refers to the number of seismic events with moment above the corresponding  $M$ .

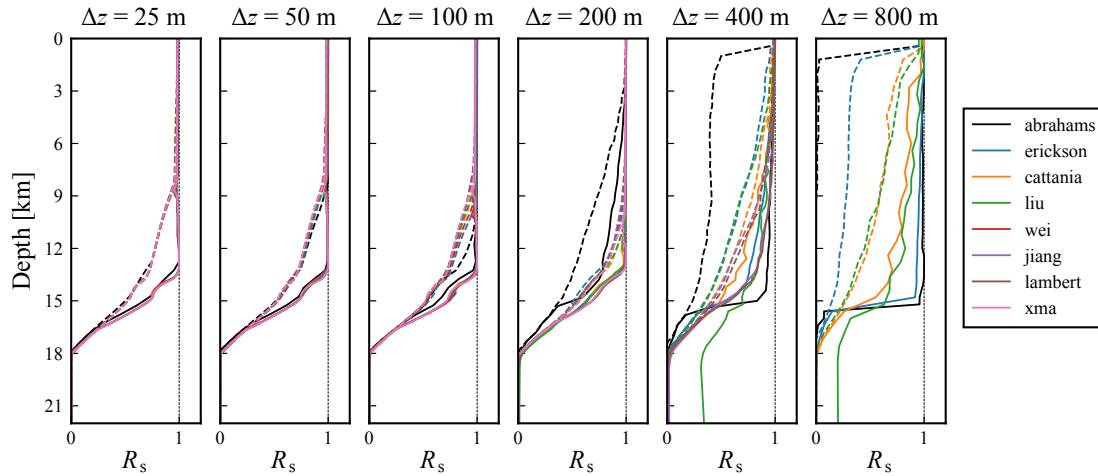


Figure 10: Effect of model resolution on seismic-aseismic slip partitioning over depth. Depth distribution of the ratio of total seismic moment release to total moment release,  $R_s$ , is shown by solid lines. The ratio between seismic moment due to surface-breaching earthquakes (with surface slip greater than 0.1 m) to total moment release is indicated by dashed lines. Simulations with different resolutions are shown, with the same color for each modeling group. Note that not all groups have simulation results for all resolutions.

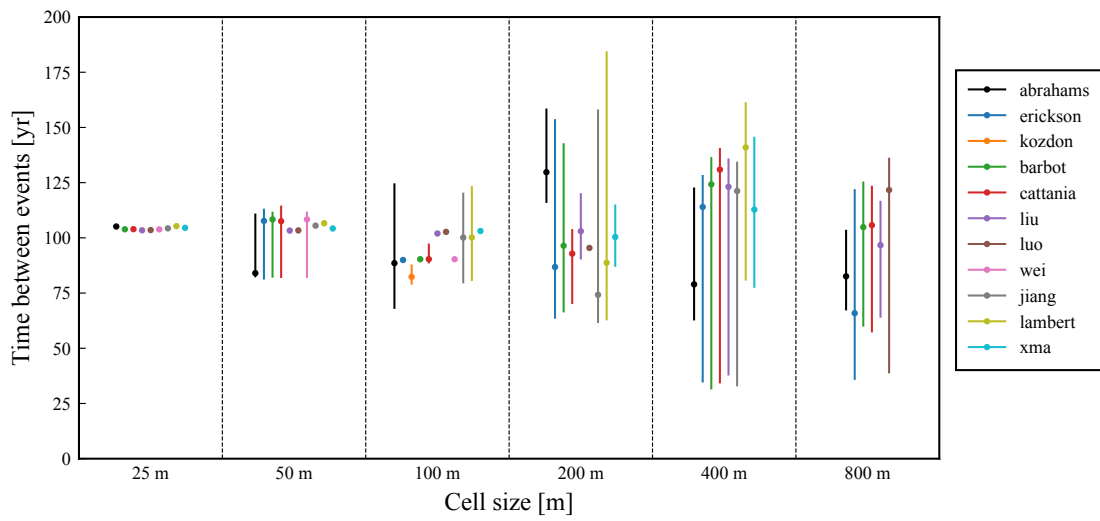


Figure 11: Effect of model resolution on recurrence intervals of large surface-breaching events. The vertical lines indicate the range of recurrence interval values, with the median value marked as dots.